A spectral scheme for the simulation of dynamic mode 3 delamination of thin films

Julien M. Hendrickx [a], Philippe H. Geubelle [b,*], Nancy R. Sottos [c]

[a] *Départment d'Ingénierie Mathématique, Université Catholique de Louvain, 1348 Louvain-la-Neuve, Belgium*
[b] *Department of Aerospace Engineering, University of Illinois at Urbana-Champaign, Urbana, IL 61801, USA*
[c] *Department of Theoretical and Applied Mechanics, University of Illinois at Urbana-Champaign, Urbana, IL 61801, USA*

Abstract

Motivated by recent developments in laser-induced spallation testing of thin film structures, we develop a spectral scheme for the simulation of dynamic failure of thin films. In this first study, we focus on the anti-plane shear (mode 3) loading case. The scheme relies on an exact spectral representation of the elastodynamic solutions in the substrate and in the film, and their combination through interface conditions that involve general cohesive failure and/or frictional contact models. A detailed modal analysis of the response of a single spectral mode is performed to assess the stability and precision of the resulting numerical scheme. A set of dynamic fracture problems involving non-propagating and propagating cracks are simulated to show the ability of the numerical scheme to capture the effect of wave reflection on the near-tip stress and displacement fields, and on the dynamic motion of a crack along the film/substrate interface.
© 2005 Elsevier Ltd. All rights reserved.

Keywords: Spectral scheme; Thin film; Delamination; Dynamic fracture; Spallation

1. Introduction

Thin film applications are increasingly prevalent in engineering applications. They are crucial components in a wide range of multilayer micro-electronic and optical devices and are also desirable candidates for micro-actuators in micro-electro-mechanical devices. In the design of such devices, adhesion is a critical parameter governing the mechanical behavior and reliability of a thin film on a substrate. Understanding

---

* Corresponding author. Tel.: +1 217 244 7648; fax: +1 217 244 0720.
  E-mail address: geubelle@uiuc.edu (P.H. Geubelle).

the possible propagation of the delamination cracks along the interface between the thin film and the substrate and extracting the interface failure properties are therefore very important.

Significant effort has been devoted to the development of test procedures for the measurement of thin-film adhesion, of which the most common are the scratch, peel, pull, blister, and indentation tests. All these tests subject the interface to high stress levels that result in significant plastic deformation [1–3]. The stress fields are difficult to analyze and the resulting measurements tend to be qualitative and not well correlated to the fracture energy. Zhuk et al. [4] used an alternative version of the peel test known as the superlayer delamination test to study the interface fracture energy between micro-molded epoxy films and self-assembled monolayers on Au/Ti/Si substrates. The superlayer test requires fairly complex sample preparation and is limited to films in which the adhesion to the substrate is weaker than to the superlayer. Inelastic dissipation induced in the films during the test makes correlation between the surface chemistry, the work of adhesion and the fracture energy difficult.

In contrast to the adhesion tests described above, laser spallation techniques [5–7] dynamically load the interface in a precise, non-contacting manner using laser-generated stress waves. Because of the rapid loading, inelastic deformations are much smaller than in quasi-static tests. This technique has been used to measure the tensile strength of a wide range of thin film/substrate interfaces [8]. More recently, Wang et al. carried out a systematic parametric study of tensile spallation and extended the method to mixed-mode loading of thin film interfaces [9–13].

The basics of stress wave generation in the tensile loading spallation experiment are summarized in Fig. 1. The sample consists of a transparent confining layer, a thin energy-absorbing layer, the substrate and the
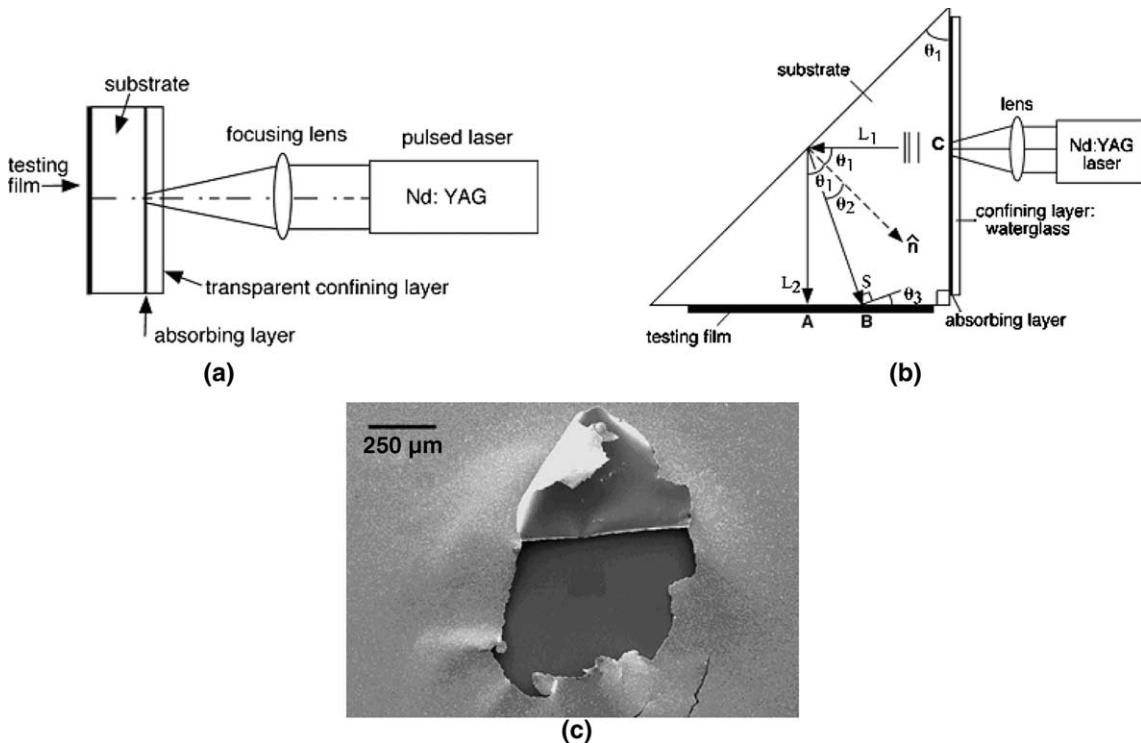

Fig. 1. (a) Schematic of the tensile laser spallation technique. (b) Schematic of the shear wave loading experiment. (c) Delamination damage of a 1 μm thick Al film on a Si substrate under tensile spallation loading [9,10,13].

testing film. An infrared, Nd:YAG pulse ($\lambda = 1064$ nm) with a variable energy content between 1 and 110 mJ, and a width of about 5 ns is incident on a metallic absorbing layer sandwiched between the confining layer and the substrate. The energy-absorbing layer is chosen to be much thicker (typically ~ 0.4 μm) than the critical penetration depth of laser light at this wavelength. A compressive longitudinal stress wave with a shape similar to that of the laser pulse is emitted from the absorbing layer. The wave that propagates towards the film–substrate interface is then reflected from the free film surface into a tensile wave, which then loads the testing interface in tension. The laser energy is increased until a longitudinal wave is generated with amplitude sufficient to fail the film/substrate interface. Typical damage for tensile loading of an Al film/fused Si substrate is shown in Fig. 1c. Mixed-mode loading of the thin film interface can be achieved in a similar fashion by modifying the planar tensile substrate to a triangular prism (Fig. 1b). A high-amplitude, short-duration shear wave is generated by mode conversion at the oblique surface and then allowed to impinge the test film.

The analysis supporting these laser-induced spallation experiments has so far been based on the propagation of 1-D waves [13]. Interferometric measurements of out-of-plane displacement are made at the surface of the testing film. From displacement measurements at the free surface, u^H, the stress history at the interface is inferred using standard wave mechanics and the maximum stress acting on the interface is calculated. However, this assumption breaks down as soon as the initial failure takes place, since the problem then becomes 2-D or 3-D. More advanced tools are thus needed and the development of such a tool is the primary objective of this work.

In the simulation of fracture propagation in infinite media, the spectral formulation has proven to be one of the most efficient tools currently available. It was used to analyze the behavior of a fracture propagating in an infinite 2-D medium under an anti-plane shear loading [14], or at the interface between two different semi-infinite materials [15]. It also provides a very efficient way to analyze the dynamic propagation of planar cracks in a 3-D infinite material [16] or at the interface between two semi-infinite materials [17]. The objective of this project is to propose a spectral formulation to simulate the thin film dynamic delamination problem. In this initial "feasibility study", we only consider the mode III problem, i.e., the case of an anti-plane shear loading. This problem is chosen because, although it captures many of the wave propagation characteristics of the in-plane cases, its mathematical treatment is somewhat simpler.

The next section provides a description of the dynamic fracture problem to be solved, followed, in Section 3, by the derivation of the spectral formulation of the elastodynamic solution for the substrate and film, and of the interface conditions used to link these two solutions. Details on the implementation of the spectral scheme are provided in Section 4, together with a stability and precision study, referred to as the modal analysis, in which we analyze the response of a single spectral mode. Sections 5 and 6 present the solution of thin film fracture problems involving non-propagating and propagating interfacial cracks. Through these examples, we demonstrate the precision with which the spectral scheme is able to capture how the finite thickness of the film affects the transient near-tip fields and the motion of the delamination crack.

2. Problem description

As alluded to in the previous, the basic objective of this paper is to develop a spectral scheme to analyze the behavior of a dynamic fracture event that takes place at the interface between a semi-infinite linearly elastic substrate and a linearly elastic thin film of thickness H when this interface is loaded by an anti-plane plane shear plane wave coming from the substrate $\tau^B(t)$. To be more general, we also consider that the surface of the film is subjected to a time- and space-dependent anti-plane shear load $\tau^H(x, t)$ (Fig. 2). The approach adopted hereafter relies on the *independent spectral formulation* used in [15] to solve dynamic interface fracture problems: we first derive a spectral form of the boundary integral relation between the
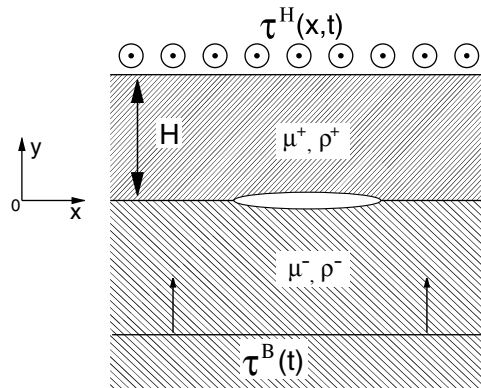
Fig. 2. Geometry of the mode III thin film delamination problem.

traction stress and the associated displacement along the interface for both subdomains, and then link these relations with a cohesive failure model.

Let us define a Cartesian coordinate system such that the interface is given by $y = 0$ (Fig. 2). Inside both domains, following the anti-plane shear-assumption, the only non-vanishing displacement component $u_z(x, y, t)$ is independent of the z-coordinate and satisfies the scalar wave equation

$$c_s^2(u_{z,xx} + u_{z,yy}) = \ddot{u}_z, \tag{1}$$

where a superposed dot means a derivation with respect to the time, and $*_{,\alpha}$ means $\frac{\partial *}{\partial \alpha}$. The shear wave speed c_s that appears in the previous equation is given by

$$c_s = \sqrt{\frac{\mu}{\rho}},$$

where μ denotes the shear modulus and ρ the density. We use (μ^+, ρ^+, c_s^+) for the thin film, (μ^-, ρ^-, c_s^-) for the substrate, and (μ, ρ, c_s) when the equation can be applied to both domains. The same convention is used for the displacement and stress fields.

The boundary condition along the surface of the film is

$$\tau^H(x, t) = \mu^+ u_{z,y}^+ \quad (x, y = H, t), \tag{2}$$

and quiescent initial conditions are assumed in the film and in the substrate prior to the arrival of the plane wave $\tau^B(x, t)$ and/or the surface load $\tau^H(x, t)$.

3. Spectral formulation

If $\Omega(y, t; q)$ is the Fourier transform of $u_z(x, y, t)$ with respect to the x-coordinate, (1) becomes

$$\ddot{\Omega} = c_s^2(-q^2 \Omega + \Omega_{,yy}).$$

Taking a Laplace transform with respect to time, we rewrite the wave equation as the following ordinary differential equation (ODE):

$$\widehat{\Omega}_{,yy} = q^2 \alpha_s^2 \widehat{\Omega},$$

where $\widehat{\Omega} = \mathscr{L}(\Omega)$ and

$$\alpha_s = \sqrt{1 + \frac{p^2}{q^2 c_s^2}}.$$

The general solution of this linear ODE is given by

$$\widehat{\Omega}(y; p, q) = \widehat{A}(p, q) e^{|q|\alpha_s y} + \widehat{B}(p, q) e^{-|q|\alpha_s y}. \tag{3}$$

In this spectral boundary integral formulation, we are primarily interested in the solution along the interface plane, i.e., in the interface displacement $u(x, t)$ and traction stress $\tau(x, t)$ defined as

$$\begin{cases} u(x, t) = u_z(x, y = 0, t), \\ \tau(x, t) = \mu\, u_{z,y}(x, y = 0, t). \end{cases}$$

Using (3), these relations become in the Fourier/Laplace domain

$$\begin{cases} \widehat{U} = \widehat{A} + \widehat{B} \\ \widehat{T} = \mu|q|\alpha_s \widehat{A} - \mu|q|\alpha_s \widehat{B}. \end{cases} \tag{4}$$

The additional relation needed to link $\widehat{T}$ and $\widehat{U}$ is provided by the condition at $y \to -\infty$ for the substrate and at $y = H$ for the thin film, as described in the next two sections.

3.1. Solution in the substrate

To keep the value of u_z bounded when $y \to -\infty$, we take $\widehat{B} = 0$ in (3) and eliminate $\widehat{A}$ in (4) to obtain

$$\widehat{T}^- = \mu^- |q| \alpha_s^- \widehat{U}^-,$$

which can be reformulated by extracting the so-called *radiation term* [16] as

$$\widehat{T}^- = \frac{\mu^-}{c_s^-} p \widehat{U}^- + \mu^- |q| \left(\alpha_s^- - \frac{p}{|q| c_s^-} \right) \widehat{U}^-. \tag{5}$$

In the time domain, the relation between the traction stress and the displacement along the interface takes the form

$$T^-(t; q) = \frac{\mu^-}{c_s^-} \dot{U}^-(t; q) + F^-(t; q), \tag{6}$$

where F^- denotes the result of the convolution of U^- and the inverse Laplace transform of the term in parenthesis in (5),

$$F^-(t; q) = \mu^- |q| \int_{-\infty}^{t} C_\infty(|q| c_s^- t') U^-(t - t'; q) |q| c_s^-\, dt'. \tag{7}$$

The convolution kernel is defined by

$$C_\infty(T) = \mathscr{L}^{-1}\left(\sqrt{1 + s^2} - s \right) = \frac{J_1(T)}{T}, \tag{8}$$

where J_1 denotes the Bessel function of the first kind and is plotted in Fig. 3.

An inverse Fourier transform back in the space domain yields the desired relation between u^- and τ^-:

$$\tau^-(x, t) - \frac{\mu^-}{c_s^-} \dot{u}^-(x, t) = f^-(x, t) + 2\tau^B(t) \doteq l^-(x, t), \tag{9}$$

where $f^-(x, t) = \mathscr{F}^{-1}(F^-(t; q))$ denotes the convolution term, and where the term $2\tau^B(t)$ is introduced to represent the shear wave coming from the substrate. The factor "2" can be justified by the fact that, in
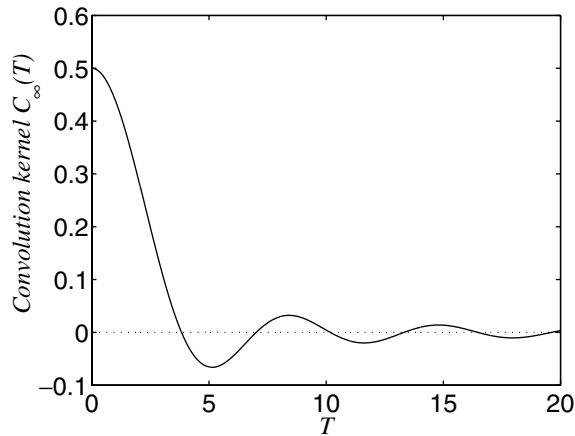
Fig. 3. Convolution kernel for the substrate $C_\infty(T)$.

the absence of any interface motion ($\dot{u}^- = 0$), the traction along the (rigid) interface is equal to twice the amplitude of the plane stress wave $\tau^B(t)$.

3.2. Solution in the thin film

In the Fourier/Laplace domain, the boundary condition (2) is expressed as

$$\widehat{T}^H(q,p) = \mu^+ \widehat{\Omega}_{,y}(y = H; p, q).$$

Using this relation and (3) to eliminate $\widehat{A}$ and $\widehat{B}$ in (4) yields

$$\widehat{T}^+ = -\mu^+ |q| \alpha_s^+ \tanh(a\alpha_s^+) \widehat{U}^+ + \frac{1}{\cosh(a\alpha_s^+)} \widehat{T}^H, \tag{10}$$

where α_s was introduced in the previous section and the non-dimensional wave number a is defined by

$$a = |q|H.$$

The extraction of the radiation term and the inversion in the time domain of the two-convolution formulation (10) are described in Appendix A. As shown there, the presence of sums of exponential functions in the denominators of the two convolution terms on the right-hand side of (10) leads to non-decaying convolution kernels with an infinite number of jumps associated with the wave reflections off the film surface.

To eliminate the numerical complexity associated with these non-vanishing kernels, we multiply (10) by $(1 + e^{-2\alpha_s^+ a})$ to get

$$\left(1 + e^{-2\alpha_s^+ a}\right) \widehat{T}^+ = \mu^+ |q| \alpha_s^+ \left(e^{-2\alpha_s^+ a} - 1\right) \widehat{U}^+ + 2e^{-\alpha_s^+ a} \widehat{T}^H.$$

Back in the time and space domain, this relation yields the following *three-convolution spectral formulation*:

$$\frac{\mu^+}{c_s^+} \dot{u}^+(x,t) + \tau^+(x,t) = \frac{\mu^+}{c_s^+} \dot{u}^+\left(x, t - 2\frac{H}{c_s^+}\right) + f^+(x,t) - \tau^+\left(x, t - 2\frac{H}{c_s^+}\right) - g^+(x,t)$$

$$+ 2\tau^H\left(x, t - \frac{H}{c_s^+}\right) + h^+(x,t) \doteq l^+(x,t), \tag{11}$$

where the three convolution terms are given in the Fourier domain by

$$
\begin{cases}
F^+(t;q) = -\mu^+|q|aU^+\left(t - 2\frac{H}{c_s^+};q\right) + \mu^+|q|\int_0^t \left\{-C_\infty(|q|c_s^+t') + C_{H3}(|q|c_s^+t')\right\}U^+(t - t';q)|q|c_s^+\,\mathrm{d}t', \\
G^+(t;q) = -\int_0^t D_3(|q|c_s^+t')T^+(t - t';q)|q|c_s^+\,\mathrm{d}t', \\
H^+(t;q) = -\int_0^t E_3(|q|c_s^+t')T^H(t - t';q)|q|c_s^+\,\mathrm{d}t'.
\end{cases}
$$

$$(12)$$

The newly introduced kernels are obtained in a way similar to that used in Appendix A and are given by

$$
\begin{cases}
C_{H3}(T) = \left(\dfrac{J_1\left(\sqrt{T^2-4a^2}\right)}{\sqrt{T^2-4a^2}} + 4a^2\dfrac{J_2\left(\sqrt{T^2-4a^2}\right)}{T^2-4a^2}\right)H(T - 2a), \\
D_3(T) = 2a\dfrac{J_1\left(\sqrt{T^2-4a^2}\right)}{\sqrt{T^2-4a^2}}H(T - 2a), \\
E_3(T) = 2a\dfrac{J_1\left(\sqrt{T^2-a^2}\right)}{\sqrt{T^2-a^2}}H(T - a).
\end{cases}
$$

$$(13)$$

As shown in Fig. 4, these kernels contain only one jump and rapidly decay to zero when the value of T increases. As expected, the kernels of the convolution terms involving interface quantities (C_{H3} and D_3) takes non-zero values only after $T = 2a$, which corresponds to the time needed for a wave to cross the thin film twice. On the other hand, the kernel E_3, which is convoluted with the applied surface traction T^H, experiences its jump at $T = a$ since the shear wave needs only to cross the film once to reach the interface. The same comment can be made about the terms $u^+(x, t - 2H/c_s^+)$, $\tau^+(x, t - 2H/c_s^+)$ and $\tau^H(x, t - H/c_s^+)$ appearing in (11).
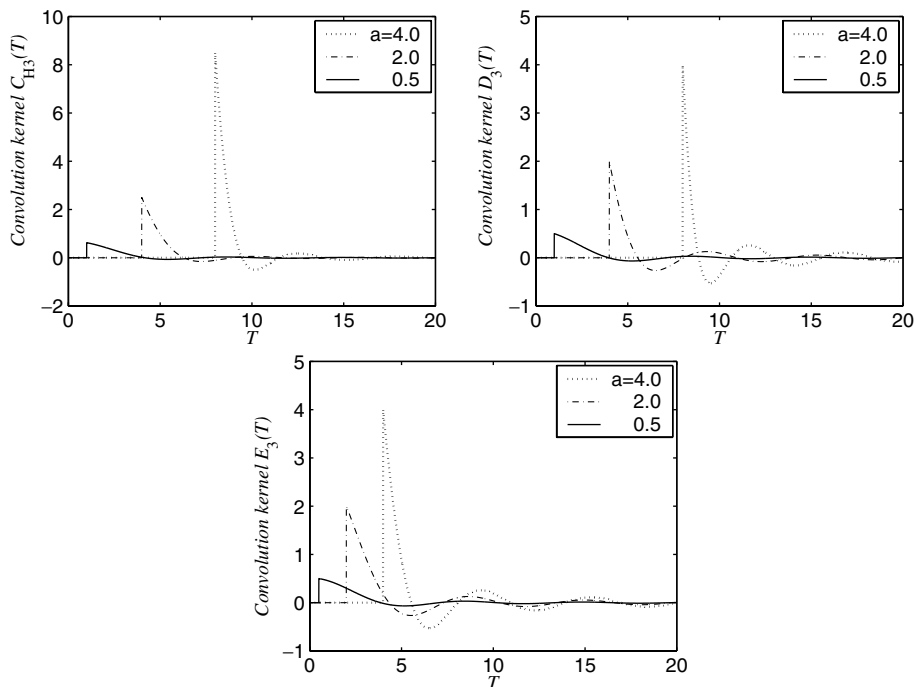

Fig. 4. Convolution kernels $C_{H3}(T)$, $D_3(T)$ and $E_3(T)$ entering the *three-convolution* spectral formulation of the thin film solution for three values of a. The kernels exhibit only one discontinuity and decay rapidly to zero.

3.3. Cohesive failure model

After deriving independent relations in the thin film and the substrate between the traction stress $\tau^\pm(x,t)$ and the displacement $u^\pm(x,t)$ along the interface and their history, we now link these two elastodynamic solutions by a cohesive interface failure model, in accordance with the *independent spectral formulation* introduced in [15].

The cohesive model starts with the enforcement of traction continuity along the interface: $\tau^+ = \tau^- = \tau$. To model the failure process itself, we introduce the failure strength distribution τ_{str} along the interface, i.e., the maximum allowable value of the interface traction stress τ. As shown in [16], the spectral scheme allows for the incorporation of a wide range of cohesive failure and friction models as τ_{str} can depend on current and previous values of the slip and slip rate and the coordinate x for spatially non-uniform failure models. In this paper, we adopt a simple linearly decreasing rate-independent model described by

$$\tau_{str} = \tau_{str0}\left(1 - \frac{|\delta|}{\delta_c}\right)H(\delta_c - |\delta|), \tag{14}$$

where $\delta(x,t) = u^+(x,t) - u^-(x,t)$ denotes the displacement jump or slip across the fracture plane, and where the value of the critical slip δ_c and the initial strength τ_{str0} characterize the failure properties of the interface. To prevent the fracture surfaces from re-adhering, the strength is only allowed to decrease. For this model, the fracture toughness G_c defined as the area under the traction-separation law is given by $\frac{1}{2}\tau_{str0}\delta_c$.

The traction stress along the interface can thus be determined by resolving the linear system provided by (9) and (11)

$$\begin{cases} \tau(x,t) - \frac{\mu^-}{c_s^-}\dot{u}^-(x,t) = l^-(x,t), \\ \tau(x,t) + \frac{\mu^+}{c_s^+}\dot{u}^+(x,t) = l^+(x,t), \end{cases} \tag{15}$$

assuming first that $\dot{u}^-(x,t) = \dot{u}^+(x,t)$. If the computed traction stress is larger than the strength given by (14), one replaces $\tau(x,t)$ by $\tau_{str}(x,t)$ and reintroduces this value in (15) to compute the interface velocities $\dot{u}^-(x,t)$ and $\dot{u}^+(x,t)$.

4. Implementation and stability issues

4.1. Implementation

To implement the spectral formulation derived in the previous section, we need to discretize and limit the space and the frequencies. We consider thus the behavior of the interface on a length X represented by $N + 1$ equidistant points, which implies a gap $\Delta x = \frac{X}{N}$ between two consecutive points. To link the space domain and the frequency domain, we use a Discrete Fourier Transform and Inverse Transform, which automatically sets the discretization of the frequency domain,

$$q_0 = \frac{2\pi}{X}, \quad q_j = jq_0, \quad j = 1,\dots,N/2, \qquad q_{max} = \frac{2\pi}{\Delta x},$$

where q_{max} is the maximal frequency and q_0 is the smallest frequency and the discretization gap. Since all the used frequencies are integers multiple of q_0, the use of a discrete Fourier transform also implies that the problem that is really solved is periodic and results in an infinite juxtaposition of domains of length X [18].

Time is also discretized using a uniform time step size Δt. The interface velocities obtained from (15) are integrated with the aid of an explicit first-order scheme. The time step size Δt is thus dictated by the CFL condition $\beta < 1$, where

$$\beta \Delta x = \max(c_s^+, c_s^-) \Delta t.$$

A summary of the spectral scheme implementation is provided in the algorithm listed below, where $*_{(j,i)}$ denotes $*(x_j, t_i)$, and $*_{(i;k)}$ denotes $*(t_i, q_k)$

```
for each i do (loop over time steps)
    Perform FFT on (u⁺, u⁻)₍∗,ᵢ₎, τ₍∗,ᵢ₎, τᴴ₍∗,ᵢ₎
    for each k do (loop over spectral modes)
        Compute the convolution terms in the Fourier domain
        L⁺₍ᵢ;ₖ₎, L⁻₍ᵢ;ₖ₎ using (7) and (12)
    end do
    Perform the IFFT: (l⁺, l⁻)₍∗;ᵢ₎ = FFT⁻¹(L⁺, L⁻)₍ᵢ,∗₎
    for each j do (loop over spatial sampling points)
        Solve (15) assuming u̇⁺₍ⱼ,ᵢ₎ = u̇⁻₍ⱼ,ᵢ₎
        Use (14) to compute τₛₜᵣ(u⁺₍ⱼ,ᵢ₎ − u⁻₍ⱼ,ᵢ₎)
        if |τ₍ⱼ,ᵢ₎| > τₛₜᵣ then
            τ₍ⱼ,ᵢ₎ := τₛₜᵣ
            Compute (u̇⁺, u̇⁻)₍ⱼ,ᵢ₎ using (15)
        end if
        Update (u⁺, u⁻)₍ⱼ,ᵢ₊₁₎ = (u⁺, u⁻)₍ⱼ,ᵢ₎ + (u̇⁺, u̇⁻)₍ⱼ,ᵢ₎ · Δt
    end do
end do
```

4.2. Modal analysis

To assess the accuracy and stability of the spectral scheme described above, we now turn our attention to the solution of a special loading case for which a closed-form solution exists for the interface quantities. This special problem involves a surface loading with a single mode

$$\tau^H(x,t) = \tau_0^H e^{iqx} H(t),$$

and a perfect interface ($\tau_{str} = \infty, u^+ = u^- = u$) between materials having possibly different stiffness ($\mu^+ \neq \mu^-$) but the same shear wave speed ($c_s^+ = c_s^- = c_s$). Writing the interface displacement and the traction stress as $(u(x,t), \tau(x,t)) = (U(t), T(t)) e^{iqx}$ and eliminating T in (5) and (10) yield, in the Laplace domain,

$$\tau_0^H = pq \widehat{U} (\mu^- \alpha_s \cosh(\alpha_s a) + \mu^+ \alpha_s \sinh(\alpha_s a)).$$

Back in the time domain and using the discretized time $t = i\Delta t$, the analytical expression for the non-dimensional interface velocity $r(i)$ can be shown to be

$$r(i) = \frac{\dot{U}(i\Delta t)}{\dot{U}\left(\frac{H}{c_s \Delta t}\right)} = \sum_{n=0}^{\infty} \left(\Delta_\mu^n J_0 \left(a \sqrt{\left(\frac{i}{\eta}\right)^2 - (2n+1)^2} \right) H\left(\frac{i}{\eta} - (2n+1)\right) \right), \tag{16}$$

where J_0 is the Bessel function of the first kind and n denotes the number of reflections of the film surface.

In (16), we have (re-)introduced the three non-dimensional parameters entering this problem. The first one is the *relative stiffness mismatch* Δ_μ

$$\Delta_\mu = \left(\frac{\mu^+ - \mu^-}{\mu^+ + \mu^-} \right) \in [-1, 1].$$

A positive value of Δ_μ denotes a thin film stiffer than the substrate, while a negative one corresponds to a more compliant thin film. As apparent in (16), this parameter quantifies the decrease rate of the importance of the terms of the sum, and therefore of the amplitude of the jumps at each reflection, as shown in Fig. 5. The second parameter is the aforementioned *non-dimensional wave number a*

$$a = |q|H,$$

which influences the behavior of the solution between the jumps. For small values of the non-dimensional wave number, the solution is essentially flat, while, for large values, it shows persistent oscillations, as shown in Fig. 5. The last parameter is the *time-discretization factor* η

$$\eta = \frac{H}{c_s \Delta t},$$

that represents the number of time steps needed for a wave to cross the thin film. Its value does not influence the shape of the solution, but only the precision of the discretization. Furthermore, for a same number of shear wave reflections, its value determines the total number of time steps.

Fig. 6 shows an example of comparison between the analytical solution described by (16) and the numerical results obtained with the spectral scheme summarized in the previous section. As illustrated in this figure, excellent agreement is achieved for small values of the time step Δt (i.e., for large values of the non-dimensional parameter η), but numerical errors may rise for larger values of η.

To quantify the error, we use the internal mean square error computed on each period of time n corresponding to the time between the nth and the $(n + 1)$th reflections of the wave off the interface,

$$E_X^2(n) = \frac{c_s^+}{2X(1 - \zeta)H} \int_X \int_{(-1 + \zeta + 2n)\frac{H}{c_s^+}}^{(1 - \zeta + 2n)\frac{H}{c_s^+}} |\dot{u}(x, t) - \tilde{\dot{u}}(x, t)|^2 \, dt \, dx,$$

where $\dot{u}(x, t)$ is the exact interface velocity and $\tilde{\dot{u}}(x, t)$ is the velocity computed by the numerical simulation. The purpose of the parameter $\zeta \in [0, 1]$ is to avoid the influence of some large errors taking place just after
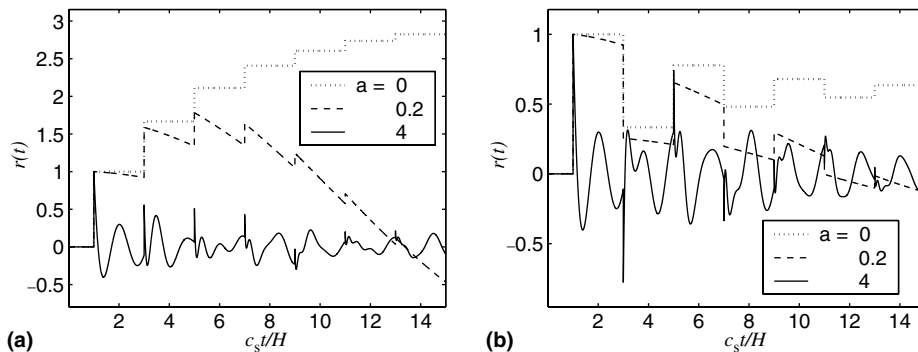

Fig. 5. Exact solution of the single mode problem: evolution of the non-dimensional interface velocity $r(t)$ for various values of a when $\Delta_\mu = 2/3$ (a) or $\Delta_\mu = -2/3$ (b). For the spatially uniform loading case ($a = 0$), the velocity converges to $\tau_0^H c_s / \mu^-$ in a monotonic way when $\Delta_\mu > 0$ and in an alternating way when $\Delta_\mu < 0$.
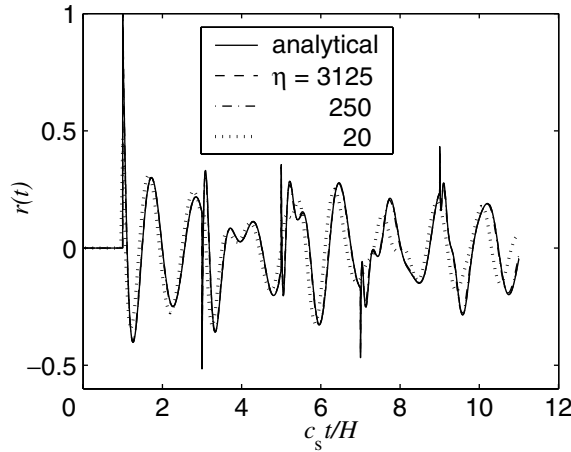
Fig. 6. Modal analysis: comparison of analytical and numerical solutions for the evolution of the non-dimensional interface velocity $r(t)$ with $a = 4.995$ and $\Delta_\mu = -2/3$. The numerical solutions are presented for three values of the non-dimensional time step size η, showing excellent match for smaller time step sizes (i.e., for larger values of η) and a decrease in precision for $\eta = 20$.

or before the reflections, due for example to a small delay between the jump in the analytical solution and the jump in the result of the numerical simulation. A value $\zeta = 0.2$ is typically adopted. The main advantage of this error measure appears in the case of a constant loading (in time) of the thin film with a perfect (i.e., non-failing) interface or in the limiting case of a free-standing thin film. In that case, if we neglect the error caused by the FFT, it can indeed be shown that the error $E_X^2(n)$ is the weighted sum of the square error on all the space-modes involved in the simulation, with the weight of mode q given by $\left| \dot{U}\left(\frac{H}{c_s^+}; q\right) \right|^2$.

Fig. 7 presents the dependence on η of the non-dimensional least square error ϵ defined by

$$\epsilon^2(n) = \frac{1}{2(1-\zeta)\frac{H}{c_s^+}} \int_{(-1+\zeta+2n)\frac{H}{c_s^+}}^{(1-\zeta+2n)\frac{H}{c_s^+}} (r(t) - \tilde{r}(t))^2 \, \mathrm{d}t.$$
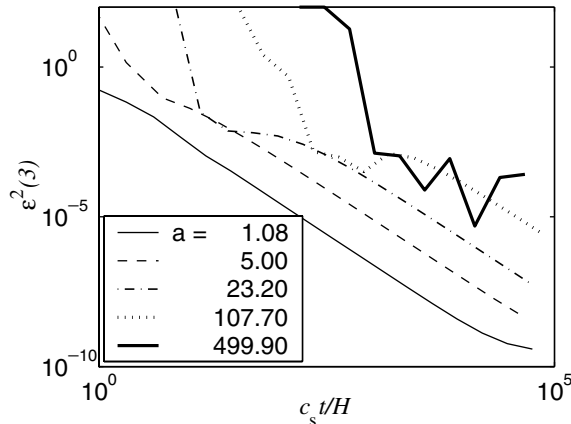

Fig. 7. Internal mean square error of the third period $\epsilon^3(3)$ versus η for five values of a and for $\Delta_\mu = -2/3$, showing the $1/\eta$ dependence of the error and the instability associated with large spectral modes.
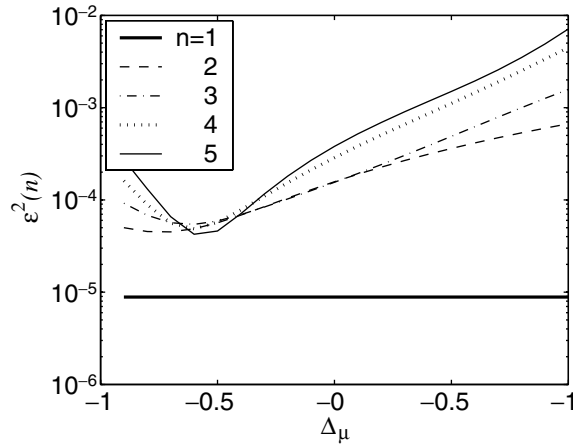
Fig. 8. Internal mean square error $\epsilon^2(n)$ versus Δ_μ for $a = 50$, $\eta = 5000$ and for different wave reflection periods n, with $n = 1$ denoting the time period between the arrival of the first loading wave and that of its first reflection off the film surface. The results show that the error increases with the number of wave reflections n, and that $\Delta_\mu = 0$ is not optimal from the error analysis point of view.

As apparent in this figure, the evolution of the error is linear with η^{-1} for a large set of values of the parameters (a, η) and the error is larger for the higher spectral modes (i.e., for larger values of a), with the behavior observed for large values of a indicating possible instability. As illustrated in Fig. 8, larger values of Δ_μ also imply a larger error, but this effect is hard to characterize and the dependence is not always monotonous. However, it is interesting to notice that the case $\Delta_\mu = 0$, corresponding to two materials with the same properties for the film and the substrate, is not optimal from the point of view of the error analysis. We can also see that the error usually increases with the period n, especially when its value is already large.

For large values of a, the solution becomes unstable after a few periods and eventually diverges totally. It is obvious that increasing η (i.e., reducing the time step size) delays the appearance of these instabilities, but it is not clear if one can always find a value of η such that the problem is always stable, or if one can always find a number of periods after which the simulation diverges. However, the simulation of actual systems always involves values of a such that it is impossible to avoid instabilities with an affordable time step size. This suggests the need for a stabilization procedure, as described in the next section.

4.3. Stabilization and filtering

As shown in Figs. 6 and 8, during the first period (i.e., for $\frac{H}{c_s^+} \leqslant t \leqslant 3\frac{H}{c_s^+}$), the simulation matches the analytical solution very well even when this solution experiences severe oscillations. Furthermore, for small values of a, the errors are kept relatively small. This result seems to show that the source of numerical instability is to be found in the convolution terms F^+ or G^+ defined in (12). Note that the term H^+ could also be problematic, but, since τ^H is constant in this analysis, its value is basically proportional to the mean value of E_3 on $[0, \frac{t}{|q|c_s^+}]$. This term has thus no influence on the instabilities here. However, for a varying τ^H, the behavior of H^+ would be similar to that of G^+.

Among the convolution terms, the term involving C_∞ does not lead to instability as long as the chosen time step does not violate the Courant condition, as discussed in [14,15]. The terms that can lead to instability are therefore the four Fourier terms appearing in the expression of F^+ and G^+ in (12) and (13):

$$\#1 = -\mu^+ |q| a U^+ \left(t - 2\frac{H}{c_s^+} \right),$$

$$\#2 = \mu^+ q \int_{2\frac{H}{c_s^+}}^{t} \frac{J_1\left(\sqrt{(qc_s^+ t)^2 - 4a^2} \right)}{\sqrt{(qc_s^+ t)^2 - 4a^2}} U(t - t') q c_s^+ \, \mathrm{d}t',$$

$$\#3 = \mu^+ q \int_{2\frac{H}{c_s^+}}^{t} 4a^2 \frac{J_2\left(\sqrt{(qc_s^+ t)^2 - 4a^2} \right)}{(qc_s^+ t)^2 - 4a^2} U(t - t') q c_s^+ \, \mathrm{d}t',$$

$$\#4 = 2a \int_{2\frac{H}{c_s^+}}^{t} \frac{J_1\left(\sqrt{(qc_s^+ t)^2 - 4a^2} \right)}{\sqrt{(qc_s^+ t)^2 - 4a^2}} T(t - t') q c_s^+ \, \mathrm{d}t'.$$

For a constant value of η and for large frequencies, it can be shown that the asymptotic behavior of these terms is

$$\#1 = -\frac{\mu^+}{H} a^2 U \left(t - 2\frac{H}{c_s^+} \right),$$

$$\#2 \simeq \frac{\mu^+}{H} U \left(t - 2\frac{H}{c_s^+} \right),$$

$$\#3 \simeq \frac{\mu^+}{H} a^2 U \left(t - 2\frac{H}{c_s^+} \right),$$ (17)

$$\#4 \simeq T \left(t - 2\frac{H}{c_s^+} \right).$$

The instabilities associated with the large spectral modes are thus primarily caused by terms #1 and #3. Furthermore, when $a \to \infty$, terms #1 and #3 tend to cancel each other but their absolute values tend to infinity, which leads to large truncation errors. Note that this convergence has to be considered very carefully since it implicitly assumes that U does not vary as quickly as the convolution kernels.

Since the global problems are unstable due to the high frequencies, we choose to damp these using a low-pass filter. In order to define this filter, we consider the worst possible distribution of frequencies, i.e., the slowest decreasing rate of the importance of the modes in the Fourier series, and find a filter that would keep the stability for this distribution. Since Dirac δ-functions are unlikely to appear in the displacement distribution, the worst distribution corresponds to a spatial discontinuity and can be represented by

$$u(x, t) = \sum_j e^{iq_j x} \frac{k(t)}{q_j} = \sum_j e^{\pm ia_j x/H} \frac{\check{k}(t)}{a_j}.$$

The importance of terms #1 and #3 in (17) is in this case proportional to $a/H = q$. In order to prevent the increase of these terms for high frequencies, we apply a first-order low-pass filter to the function l^+ defined in (11). So if $l^+(x, t) = \mathscr{F}^{-1}(L^+(t; q))$, we replace $L^+(t; q)$ by

$$\widetilde{L}^+(t; q) = L^+(t; q) \frac{1}{1 + \frac{q}{q_c}}.$$ (18)
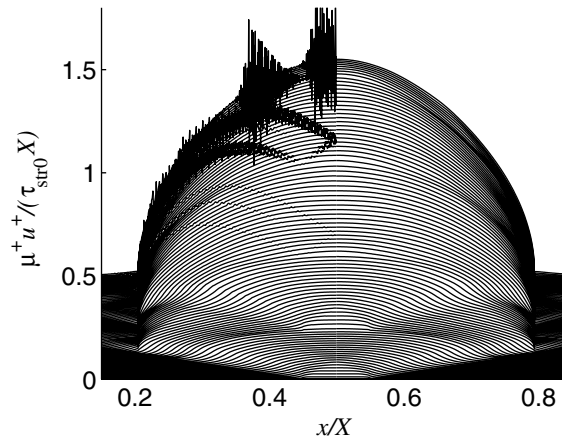
Fig. 9. Evolution of the displacement of the upper part of the interface u^+ for the problem of a crack initially located over $.45X \leqslant x \leqslant .55X$ and expanding to $.20X \leqslant x \leqslant .80X$, at which point it is arrested by an infinite interface strength. The solution plotted for $0 \leqslant x \leqslant X/2$ has been obtained without filter, while that plotted for $X/2 < x \leqslant X$ used a filter with $q_c = 1250/X$, showing how the first-order low-pass filter removes the spurious oscillations without affecting the rest of the solution.

The critical frequency q_c has to be chosen based on a trade-off between the stability and the accuracy of the numerical scheme. Since there is no theoretical way to evaluate the accuracy, we compare the solutions obtained with different critical values with those obtained without filter before the beginning of the instabilities. The results of several tests show us that applying a low-pass filter on the function $l^+(x,t)$ efficiently removes the spurious oscillations without affecting the solution, as shown in Fig. 9. However, if chosen too small, the critical frequency can lead to non-negligible errors, especially in situations involving many high frequencies. Based on the results of several tests involving non-propagating and propagating interface cracks (such as those listed in the next sections), the value $q_c = 1250/X$ appears to provide a good combination of stability and precision for the numerical results. This value is therefore adopted in the remainder of this paper. For this value of q_c, the numerical simulation is usually stable for $\beta < 0.35$, although we often adopted smaller values ($\beta = 0.05$) to achieve more precise results.

5. Non-propagating interface crack

We start the result discussion by analyzing the behavior of a non-propagating interface crack of length $L_c = 180$ μm located between a substrate made of fused silica and an aluminum thin film of thickness $H = 100$ μm loaded along its surface by a uniformly distributed anti-plane shear load $\tau^H H(t)$, where $H(t)$ denotes the Heaviside step function. These two materials, whose properties are listed in Table 1, are those used in the laser-induced spallation experiments described in [13]. The crack is prevented from propagating by imposing an infinite strength τ_{str0} outside of its initial location. The discretized portion of the interface has a length $X = (32/7)L_c \approx 823$ μm, using $\Delta x = X/1024 \approx 0.8$ μm and $\eta = H/c_s^+ \Delta t = 2048$. This implies that we satisfy the Courant condition with $\beta \approx 0.07$.

Fig. 10 shows the evolution of the slip across the interface in the crack zone. As expected, the slip is null before $t = H/c_s^+ \approx 32.28$ ns, which is the time needed for a wave to propagate from the film surface to the interface. It can also be observed that each reflection of the initial plane wave at $t = (2n+1)H/c_s^+$ corresponds to an increase of the rate of separation followed by a deceleration until the next wave reflection. To characterize the evolution of the near-tip fields, we extract the time-dependent stress intensity factor $K_{III}(t)$ that quantifies the near-tip stress singularity:

Table 1
Material properties taken from [13]

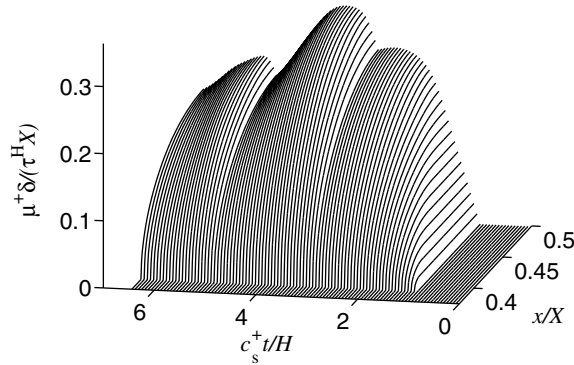| Material	μ (GPa)	ρ (kg/m^3)	c_s (m/s)
Fused silica	30.8	2200	3741.7
Aluminum	26.0	2710	3097.4

Fig. 10. Evolution between $t = 0$ and $t \approx 6.5H/c_s^+$ of the interface slip δ for the non-propagating crack problem, showing the effect of the wave reflections at $t = (2n + 1)H/c_s^+$ and the presence of a maximum at $t \approx 4H/c_s^+$.

$$\lim_{x \to x_c} \tau(x, t) = \frac{K_{\mathrm{III}}(t)}{\sqrt{2\pi|x - x_c|}}, \tag{19}$$

where $|x - x_c|$ denotes the distance from x to the crack tip. The stress intensity factor is more conveniently extracted from the evolution of the slip behind the crack tip [14]

$$K_{\mathrm{III}}(t) = \lim_{x \to x_c} \sqrt{\frac{\pi}{2|x - x_c|}} \left(\frac{1}{\mu^+} + \frac{1}{\mu^-}\right)^{-1} (u^+(x, t) - u^-(x, t)). \tag{20}$$
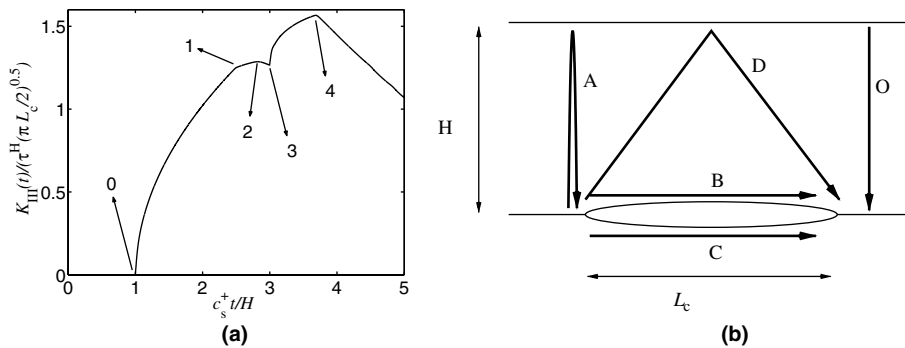

(a)   **(b)**

Fig. 11. (a) Evolution of the stress intensity factor $K_{\mathrm{III}}(t)$ for the non-moving crack problem, showing different angular points corresponding to wave reflections on the crack tips. (b) Wave propagation paths, whose transit times are $c_s^+ t_O/H = 1$, $c_s^+ t_A/H = 2$, $c_s^+ t_B/H = 1.8$, $c_s^+ t_C/H = 1.5$, and $c_s^+ t_D/H = 2.69$. The correspondence between the angular points in (a) and the different paths in (b) is presented Table 2.

Table 2
Correspondence between the angular points appearing in the evolution of $K_{III}(t)$ (Fig. 11a) and the wave propagation paths shown in Fig. 11b

Point	0	1	2	3	4
Time ($c_s^+ t/H$)	1	2.5	2.8	3	3.69
Path	O	OC	OB	OA	OD

It is important to note that the computation of the limit in (20) shows good convergence properties, which means that the spectral scheme is able to capture accurately the behavior of the interface in the neighborhood of the crack tips. As observed in Fig. 11a, the evolution of the stress intensity factor is characterized by a series of angular points corresponding to various elastodynamic reflections of waves off the crack tips. The wave propagation paths are represented in Fig. 11b. The correspondence between the wave trajectories and the angular points is presented in Table 2, showing the ability of the spectral scheme to capture the complex wave pattern that affects the near-tip stress and displacement fields. Note the strong dynamic overshoot observed at $t \approx 4H/c_s^+$.

6. Propagating delamination crack

In this section, we analyze two dynamic thin film failure problems involving the spontaneous initiation, propagation and possibly arrest of a pre-existing interfacial crack. We begin in Section 6.1 with a system composed of an aluminum thin film and a substrate made of fused silica as in the laser-induced spallation experiments of [13]. As in the experiments, the dynamic load is associated with a shear plane wave coming from the substrate. We then consider in Section 6.2 the dynamic fracture of an aluminum/steel system subjected to a sudden surface loading. Due the larger property mismatch characterizing this system, interesting failure phenomena are observed.

6.1. Dynamic delamination along Al/Si interface subjected to substrate loading

Let us consider a thin aluminum film of thickness $H = 100$ μm deposited on a fused silica substrate. The properties of the constituents are listed in Table 1. The initial crack length (i.e., the zone along the interface with zero initial strength) is $L_c = 62.5$ μm. The interface strength outside of the crack is 500 MPa in accordance to the shear strength measurements provided in [13]. The critical value of the displacement jump is chosen as $\delta_c \approx 1$ μm. The system is subjected to a plane shear wave emanating from the substrate, with an amplitude equal to $\tau_0^B = 400$ MPa. The domain size and discretization parameters adopted in the simulations are $X = 1$ mm, $\Delta x = X/1024$, $\eta = 2048$, which corresponds to $\beta = 0.06$.

Before discussing the results of the dynamic fracture simulations, it is interesting to look at the evolution of the interface stress $\tau(t)$ in the absence of a pre-existing crack. An elementary 1-D elastodynamic analysis shows that

$$\tau(t) = 2\tau_0^B \frac{1}{1 + \frac{\mu^- c_s^+}{\mu^+ c_s^-}} k^{n(t)}, \tag{21}$$

where $n(t) = \left\lfloor \frac{c_s^+ t}{2H} \right\rfloor$ and k denotes the impedance mismatch parameter defined by

$$k = \frac{\frac{\mu^+}{\mu^-} - \frac{c_s^+}{c_s^-}}{\frac{\mu^+}{\mu^-} + \frac{c_s^+}{c_s^-}} = \frac{\frac{\mu^+}{c_s^+} - \frac{\mu^-}{c_s^-}}{\frac{\mu^+}{c_s^+} + \frac{\mu^-}{c_s^-}}. \tag{22}$$

For the Al/Si system considered here, the impedance mismatch parameter is very small ($k = 0.0098$), indicating that the interface traction stress will decay rapidly to zero after just a few wave reflections of the initial wave off the film surface. After the first wave reflection, the traction stress already represents less than 1% of the initial load amplitude. This suggests that the crack propagation event is expected to be short-lived, leading to a crack arrest soon after the first reflection at $t = 2H/c_s^+$.

This expectation is confirmed in the results presented in Fig. 12, which shows the evolution of the location of the right crack tip (dash-dotted curve) and cohesive zone tip (solid curve). As expected, upon arrival of the plane wave from the substrate (time $t = 0$ denotes the arrival time of the wave at the interface), the cohesive zone starts to expand (only the right crack tip region is displayed here). Once the displacement jump reaches sufficient values (i.e., $\delta > \delta_c$), the crack tip starts to propagate rapidly and catches up with the cohesive zone tip, leading to an intersonic crack motion, as the crack speed exceeds the shear wave speed of Al (denoted by the dotted line in Fig. 12) and approaches the shear wave speed of Si (dashed line). The initial phase of the crack motion is identical to that obtained for an infinite bimaterial system. At $t = 2H/c_s^+$, however, the wave reflected off the free surface of the film hits the interface plane, which leads to the sudden slowing down of the crack. However, due to the inertia of the debonded portion of the thin film as the wave reflected off the film upper surface is again reflected off the traction-free crack faces, a stress concentration continues to persist in the crack tip region until complete crack arrest observed at $t \approx 4.8H/c_s^+$. Note also the effect of the second reflection of the initial wave at $t = 4H/c_s^+$ as the crack temporarily accelerates before coming to the final halt.

The evolution of the traction stress τ normalized by the initial strength τ_s of the interface is shown in Fig. 13. The stress is computed at three locations (labeled nodes 0, 1 and 2) along the fracture plane. At time $t = 0$, the interface is subjected to the plane wave with an amplitude equal to 80% of the strength τ_s. The observation point located the closest to the initial crack tip (node 2) then experiences an increase in τ associated with the arrival of the propagating crack tip prior to the arrival of the unloading wave reflected off the free surface. The effect of the unloading wave predicted by (21) is however clearly visible at the other two observation points (nodes 0 and 1), as the stress curves show a sharp drop to less than 1% of the initial wave amplitude. The aforementioned inertial effects associated with the debonded portion of the thin film lead, at node 1, to the a non-monotonic increase of the traction stress, which reaches the critical strength
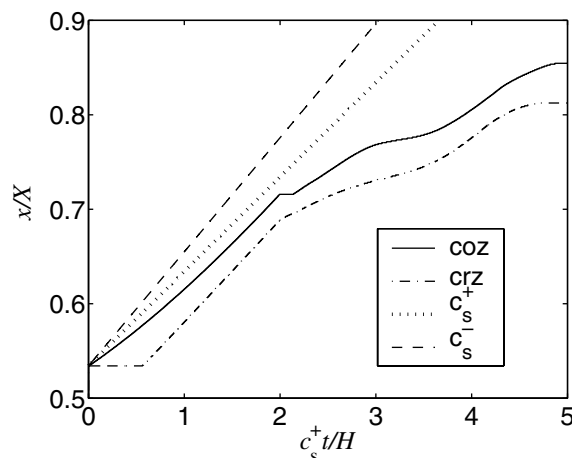

Fig. 12. Evolution of the cohesive zone tip (*coz*) and crack tip (*crz*) location for the Al/Si system loaded by a substrate wave, showing the rapid deceleration of the crack after $t = 2H/c_s^+$ and its arrest at $t \approx 4.8H/c_s^+$. The lines labeled c_s^+ and c_s^- respectively denote the propagation of elastic waves in the Al film and Si substrate.
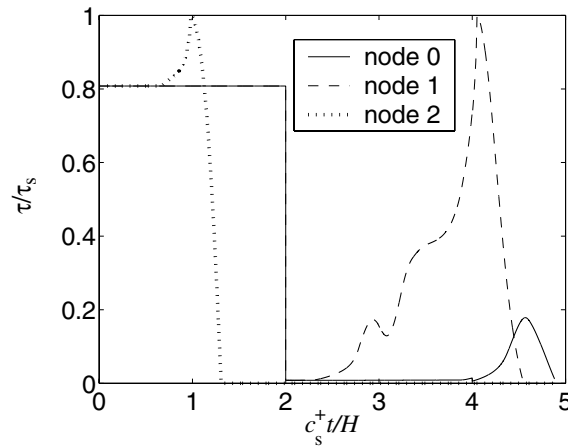
Fig. 13. Evolution of the interface stress τ (normalized by the interface strength τ_s) for the crack propagation problem shown in Fig. 12. τ is computed at three points on the fracture plane (nodes 0, 1 and 2) respectively located at 468.7, 273.4 and 78.1 μm ahead of the initial crack tip.

limit before decreasing to zero during the cohesive failure process. The farthest observation point (node 0) is located too far from the original crack tip: the stress wave emanating from the crack tip region only reaches 20% of the interface strength and is therefore insufficient to lead to its failure.

The initiation, propagation and arrest of the crack, and the effect of the reflected waves are also illustrated in Fig. 14, which presents the evolution of the normalized displacement jump or slip for $0 \leqslant x/X \leqslant 0.5$. The effect of the wave reflection at $t = 2nH/c_s^+$ is clearly visible. After the third reflection ($t > 6H/c_s^+$), the slip across the fully arrested crack decreases rapidly as the effect of the initial substrate wave disappears.

In the laser-induced spallation, the only real-time measurements during the dynamic event consist in the motion of discrete points along the film surface. To that effect, the spectral formulation has been extended in Appendix B to allow for the direct computation of the motion of the thin film surface. The evolution of the velocity $\dot{u}^H$ is presented in Fig. 15 for four points located on the film surface. The first point, labeled $x = 0$, (dotted curve) is located directly above the center of the pre-existing crack; the second ($x = L_c/2$—dashed curve) is directly above the initial location of the crack tip; the last two, $x = L_c$ (dash-dotted curve)
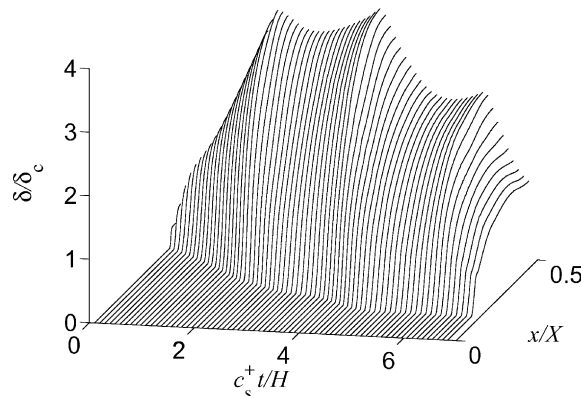

Fig. 14. Evolution of the slip δ across the Al/Si interface, showing the arrest of the crack at $t \approx 4.8H/c_s^+$. The influence of the reflections of the initial plane wave after each period of $2H/c_s^+$ is clearly visible.
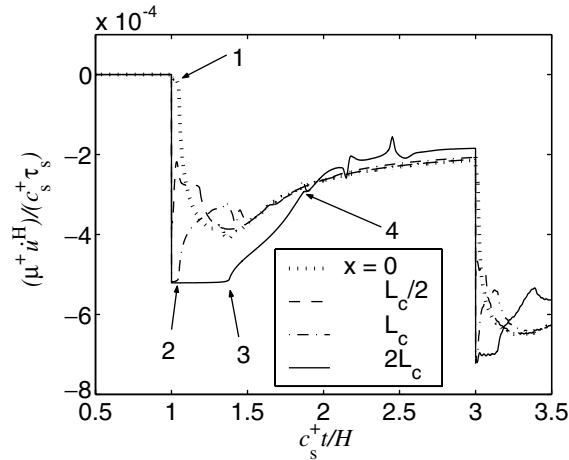
Fig. 15. Evolution of the velocity $\dot{u}^H$ at four locations along the film surface for the film failure problem presented in Figs. 12–14. $x = 0$ corresponds to the center of the pre-existing interface crack, and $x = L_c/2$ denotes the point located just above the initial crack tip. The arrows labeled 1–4 denote the arrival of the specific crack tip waves as discussed in the text.

and $x = 2L_c$ (solid curve) are located above the initially unbroken portion of the interface. All surface points undergo a fairly complex motion after the arrival of the initial wave at time $t = H/c_s^+$. As expected, the point located at $x = 2L_c$ is the last one to be affected by the interface crack, whose effect is only felt at time $c_s^+ t/H = \sqrt{1 + (3L_c/2H)^2} \approx 1.37$ (denoted by the arrow labeled "3" in Fig. 15). Prior to that, the velocity history of that surface point exhibits the sudden change at $t = H/c_s^+$ associated with the arrival of the initial loading wave and takes the constant value corresponding to an intact interface. The spectral scheme also captures the arrival at the same point of the wave emanating from the other crack tip at $c_s^+ t/H = 1.855$ (denoted by the arrow labeled "4"). The other points along the film surface experience the effect of the wave diffracted by the crack earlier. For the point located directly above the crack ($x = L_c/2$), this effect is felt at the time of arrival of the loading wave ($c_s^+ t/H = 1$). For the other two points ($x = 0$ and $x = L_c$), this effect is felt slightly later, at $c_s^+ t/H = 1.048$, as denoted by the arrows labeled "1" and "2"). This example illustrates how the spectral scheme could be used in combination with experimental measurement to extract fracture-related information from the laser-induced spallation tests.

6.2. Spallation of a surface-loaded Al/steel system

To emphasize the role of wave reflection off the interface, we now turn our attention to the problem of a bimaterial system exhibiting a larger material mismatch, i.e., one for which the impedance mismatch parameter k defined by (22) takes a higher value. To that effect, let us consider the delamination of a 100 μm thick film made of steel deposited on an aluminum substrate. The loading considered here consists in a spatially uniform step loading $\tau^H(x,t) = \tau_0^H H(t)$ applied along the upper surface of the film. The elastic properties of the constituents are listed in Table 3. In the absence of experimental measurements of dynamic shear strength and fracture toughness of an Al/steel interface, we adopt the values $\tau_{str} = 500$ MPa and $\delta_c = 1.26$ μm. The initial crack length is 62.5 μm. The problem size is $X = 2$ mm with $\Delta x = X/1024$ and the time step size corresponds to $\eta = 1024$. The thin film is subjected to an applied surface load $\tau_0 = 625$ MPa. Since it is larger than the interface strength, this loading will lead to the complete spallation of the film. However, as seen below, due to the material mismatch along the interface, this spallation will not be instantaneous and a dynamic motion of the pre-existing crack will be observed prior to the spallation event.

Table 3
Material properties for aluminum and steel

Material	μ (GPa)	ρ (kg/m^3)	c_s (m/s)
Aluminum	26.0	2710	3097.4
Steel AISI C120	78.8	7850	3168.3

In the absence of a crack, an elementary 1-D wave analysis shows that the interface traction stress is given by

$$\tau(t) = \tau_0^H (1 - k^{n(t)}),$$

where $n(t) = \left\lfloor \frac{c_s^+ t + H}{2H} \right\rfloor$ and k denotes the impedance mismatch defined in (22), which is equal to 0.495 for the material combination of interest in this section. In the absence of a crack, the traction stress along the interface therefore evolves as follows:

$0 \rightarrow H/c_s^+$	$H/c_s^+ \rightarrow 3H/c_s^+$	$3H/c_s^+ \rightarrow 5H/c_s^+$	$5H/c_s^+ \rightarrow 7H/c_s^+$
0	$0.6307\tau_s$	$0.9432\tau_s$	$1.098\tau_s$

In other words, due the large impedance mismatch, it takes two wave reflections off the film surface before the spallation event takes place. During this time interval, the stress concentration present in the vicinity of the dynamically loaded pre-existing crack leads to the initiation and propagation of the crack, as illustrated in Figs. 16 and 17. Fig. 16 presents the evolution of the location of the right cohesive zone tip (solid curve) and crack tip (dashed curve). As expected, the cohesive zone tip starts to propagate when the loading wave hits the interface at $t = H/c_s^+$, rapidly followed by the crack tip. The effect of the first wave reflection off the film surface is clearly visible at time $t = 3H/c_s^+$ at which the cohesive zone length experiences a jump. The results also clearly show the onset of the spallation event at $t = 5H/c_s^+$, time at which the interface traction exceeds the strength along the entire interface. Complete failure of the interface is then achieved when all the points along the interface have completed their cohesive failure process.
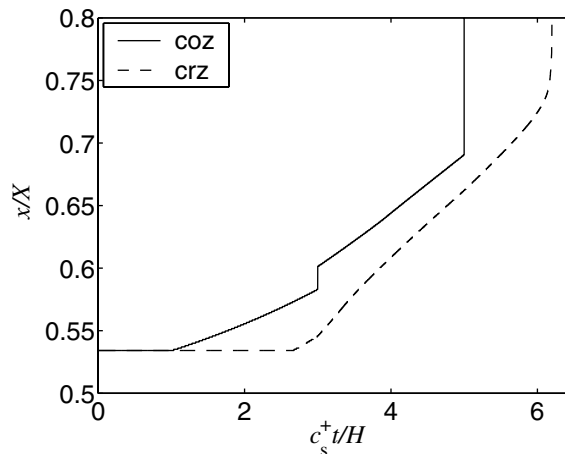

Fig. 16. Evolution of the location of the cohesive zone tip (*coz*) and crack tip (*crz*) for the Al/steel spallation problem, showing the influence on the cohesive zone of the wave reflection at $t = 3H/c_s^+$, and the spallation event beginning at $t = 5H/c_s^+$.
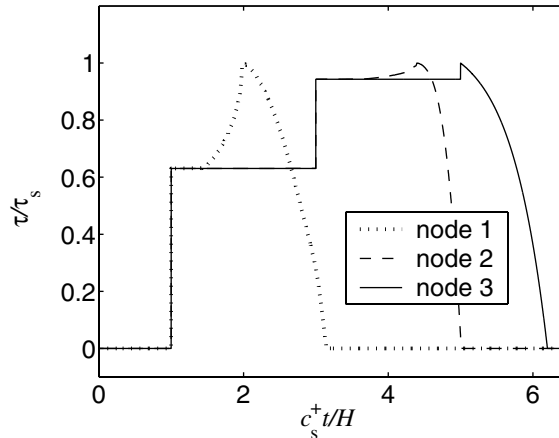
Fig. 17. Evolution of the interface stress τ for nodes 1, 2 and 3 located on the path of the propagating crack at 39, 254 and 742 μm ahead of the initial crack tip, respectively. The continuous stress rise at nodes 1 and 2 corresponds to the arrival of the propagating crack, while the discontinuous stress jump observed at node 3 at $t = 5H/c_s^+$ denotes the onset of the spallation.

The dynamic fracture/spallation process can also be visualized in Fig. 17 in terms of the evolution of the interface stress τ at three locations along the interface. A point located in the vicinity of the initial crack tip (node 1—dotted curve) experiences the stress concentration associated the propagating crack tip and completes its cohesive failure process prior to the arrival of the first reflected shear wave. For a point located further (node 2—dashed curve), the failure still takes place during the crack propagation event, prior to the arrival of the final spallation wave at $t = 5H/c_s^+$. The last point (node 3—solid curve) is located too far from the initial crack tip and only experiences the spallation process, as apparent by the discontinuous stress rise it experiences prior to its cohesive failure.

7. Conclusion

A spectral form of a boundary integral scheme has been derived to analyze the mode III dynamic delamination of thin film structures. The scheme relies on an exact spectral representation of the elastodynamic solutions in the substrate and in the film, and their combination through interface conditions that involve general cohesive failure and/or frictional contact models. The three-kernel implementation of the spectral formulation has led to a very efficient numerical scheme able to capture a wide range of dynamic failure events along the film/substrate interface, including the effect of the elastodynamic waves reflected off the film surface. The stability and accuracy of the scheme have been tested by comparing the numerical results to an analytical solution available in the case of a single mode surface loading of a perfect interface. Special emphasis was placed in that study on the effects of the time step size, material mismatch and number of reflections on the solution. The stability analysis also showed the appearance of instabilities associated with the higher spatial frequencies. To stabilize the scheme, a filter was chosen using a "worst case" frequency analysis of the different terms involved in the mathematical formulation. The use of a first-order low-pass filter in the scheme was then shown to remove the instabilities without affecting the rest of the solution.

A set of dynamic fracture problems involving non-propagating and propagating cracks was then simulated to show the ability of the numerical scheme to capture the effect of wave reflection on the near-tip stress and displacement fields. For the non-propagating crack case, the scheme was shown to provide a very

accurate description of the evolution of the stress intensity factor that quantifies the stress singularity around the crack tips. In the first delamination problem involving the initiation, propagation and arrest of a crack along an Al/Si interface, the numerical results showed the effect of the film inertia on the crack motion, as the final arrest of the crack took place after the unloading of the interface. In the final problem involving a steel/Al system subjected to a spallation surface load, the scheme was able to capture the dynamic delamination event preceding the thin film spallation.

Further studies are currently underway to better quantify the effect of the film thickness in various failure scenarios involving dynamic substrate and surface loadings, to extend the formulation to in-plane and 3-D loading conditions, and to allow for the simulation of films of finite length.

Acknowledgment

Appendix A. Laplace inversion

In this appendix, we show the Laplace inversion of the two-convolution formulation for the thin film described in the Laplace/Fourier domain by (10). The first term on the right-hand side corresponds to the displacement convolution term, while the second one, to a convolution on the applied surface loading history. The inversion of these two terms relies on the following two properties:

Property 1. If $\left(\frac{d}{c}e^{-2ks}\right) < 1$, then

$$\frac{1}{ce^{ks} + de^{-ks}} = \frac{e^{-ks}}{c}\left(\sum_{n=0}^{\infty}\left(\frac{d}{c}\right)^n e^{-2kns}\right).$$

Property 2. If

$$\mathcal{L}^{-1}(\hat{g}(s)) = g(T),$$

then

$$\mathcal{L}^{-1}\left(\hat{g}\left(\sqrt{1+s^2}\right)\right) = g(T) - \int_0^T g\left(\sqrt{T^2 - u^2}\right)J_1(u)\,\mathrm{d}u,$$

where J_1 denotes the Bessel function of the first kind.

A.1. Inversion of the displacement convolution term

Using Property 1, we obtain

$$\mathcal{L}^{-1}(s\tanh(as)) = \delta'(t) + 2\sum_{n=0}^{\infty}(-1)^n\delta'(t - 2na), \tag{A.1}$$

where $\delta(t)$ denotes the Dirac delta function.

Combining (A.1) and Property 2 yields

$$\mathscr{L}^{-1}\left(\sqrt{1+s^2}\tanh\left(a\sqrt{1+s^2}\right)\right) = \delta'(t) - \int_0^t v\delta'(v)\frac{J_1\left(\sqrt{T^2-v^2}\right)}{\sqrt{T^2-v^2}}\,\mathrm{d}v + 2\sum_{n=0}^{\infty}(-1)^n\delta'(t-2na)$$

$$- \int_0^t 2\sum_{n=0}^{\infty}(-1)^n v\delta'(v-2na)\frac{J_1\left(\sqrt{T^2-v^2}\right)}{\sqrt{T^2-v^2}}\,\mathrm{d}v.$$

After computation of the integrals, this relation becomes

$$\mathscr{L}^{-1}\left(\sqrt{1+s^2}\tanh\left(a\sqrt{1+s^2}\right)\right) = \delta'(t) - C_\infty(t) + 2\sum_{n=0}^{\infty}(-1)^n\delta'(t-2na)$$

$$- 2na\sum_{n=0}^{\infty}(-1)^n\delta(t-2na) + C_{H2}(t), \tag{A.2}$$

where $C_\infty(T)$ has been defined in (8), and

$$C_{H2}(t) = 2\sum_{n=1}^{\infty}(-1)^n\left(\frac{J_1\left(\sqrt{T^2-4n^2a^2}\right)}{\sqrt{T^2-4n^2a^2}} + 4a^2\frac{J_2\left(\sqrt{T^2-4n^2a^2}\right)}{T^2-4n^2a^2}\right) \tag{A.3}$$

and is plotted in Fig. 18.

Replacing s by $\frac{p}{|q|c_s^+}$ in (A.2) and performing the convolution with U^+ finally yield

$$\mathscr{L}^{-1}(-\mu^+|q|\alpha_s^+\tanh(a\alpha_s^+)\widehat{U}^+) = -\frac{\mu^+}{c_s^+}\dot{U}^+(t) - 2\frac{\mu^+}{c_s^+}\sum_{n=0}^{\infty}(-1)^n\dot{U}^+\left(t-2n\frac{H}{c_s^+}\right)$$

$$+ 2\mu^+|q|\sum_{n=1}^{\infty}(-1)^n naU^+\left(t-2n\frac{H}{c_s^+}\right)$$

$$- \mu|q|\int_0^t\left\{C_\infty(|q|c_s^+t') + C_{H2}(|q|c_s^+t')\right\}U^+(t-t')|q|c_s^+\,\mathrm{d}t'. \tag{A.4}$$
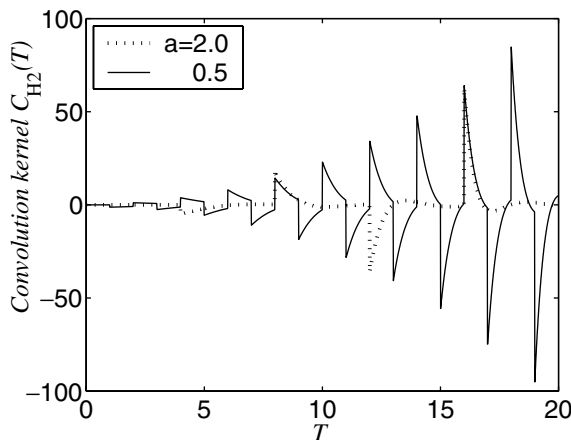

Fig. 18. Convolutions kernel $C_{H2}(T)$ appearing for the displacement U^+ in the *two-convolution* spectral formulation of the thin film solution for two values of the non-dimensional wave number a. Unlike in the *three-convolution* formulation, the kernel does not decay to zero, presents an infinite number of discontinuities at $T = 2na$, and its complexity increases with time.

A.2. Inversion of the loading convolution term

Following the same procedure, we use Property 1 to get

$$\mathscr{L}^{-1}\left(\frac{1}{\cosh as}\right) = \sum_{n=0}^{\infty}(-1)^{n}\delta(t-(2n+1)a). \tag{A.5}$$

Combining (2) and (A.5) then gives

$$\mathscr{L}^{-1}\left(\frac{1}{\cosh(a\sqrt{1+s^{2}})}\right) = 2\sum_{n=0}^{\infty}(-1)^{n}\delta(t-(2n+1)a) - 2\sum_{n=0}^{\infty}(-1)^{n}I_{n}, \tag{A.6}$$

where

$$I_{n} = \int_{0}^{t} v\delta(v-(2n+1)a)\frac{J_{1}\left(\sqrt{T^{2}-v^{2}}\right)}{\sqrt{T^{2}-v^{2}}}\,\mathrm{d}v.$$

Computing this integral, we rewrite (A.6) as

$$\mathscr{L}^{-1}\left(\frac{1}{\cosh(a\sqrt{1+s^{2}})}\right) = 2\sum_{n=0}^{\infty}(-1)^{n}\delta(t-(2n+1)a) - E_{2}(t), \tag{A.7}$$

where the new kernel

$$E_{2}(T) = 2\sum_{n=0}^{\infty}(-1)^{n}(2n+1)a\frac{J_{1}\left(\sqrt{T^{2}-(2n+1)^{2}a^{2}}\right)}{\sqrt{T^{2}-(2n+1)^{2}a^{2}}}. \tag{A.8}$$

Finally, replacing s by $\frac{p}{|q|c_{s}^{+}}$ in (A.7) and performing the convolution with T^{H} yield

$$\mathscr{L}^{-1}\left(\frac{\widehat{T}^{H}}{\cosh a\alpha_{s}^{+}}\right) = 2\sum_{n=0}^{\infty}(-1)^{n}T^{H}\left(t-(2n+1)\frac{H}{c_{s}^{+}}\right) - \int_{0}^{t}E_{2}(|q|c_{s}^{+}t')T^{H}(t-t')|q|c_{s}^{+}\,\mathrm{d}t'. \tag{A.9}$$

To conclude this appendix, let us indicate that, as apparent in Fig. 18 and in the definition (A.3) and (A.8), the convolution kernels C_{H2} and E_{2} do not decay to zero and contain an infinite number of jumps whose size increases with time. The expressions (A.4) and (A.9) also show the presence of infinite sums of terms in the two convolution terms. These infinite sums are associated with Property 1: their origin is associated with the presence of a sum of exponential functions in the denominators of the two last terms of (10).

Appendix B. Thin film surface

In the laser-induced spallation experiments described in the introductory section, interferometric measurements of the velocity history are made at discrete locations along the thin film surface. It is therefore useful to extend the spectral formulation to compute the displacement and velocity histories along $y = H$. Remembering from (3) that

$$\widehat{\Omega}(y;p,q) = \widehat{A}(p,q)\mathrm{e}^{|q|\alpha_{s}y} + \widehat{B}(p,q)\mathrm{e}^{-|q|\alpha_{s}y},$$

where $\Omega = \mathscr{L}(\mathscr{F}(u_{z}))$, and denoting the surface displacement by

$$u^{H}(x,t) = u_{z}(x,y=H,t),$$

we have

$$\widehat{U}^{H}(p,q) = \widehat{A}(p,q)\mathrm{e}^{|q|\alpha_{s}^{+}H} + \widehat{B}(p,q)\mathrm{e}^{-|q|\alpha_{s}^{+}H},$$

where $\widehat{U}^{H} = \mathscr{L}(\mathscr{F}(u^{H}))$. Using (2) and the first line of (4) to eliminate $\widehat{A}$ and $\widehat{B}$ in this last relation, we get

$$\widehat{U}^{H}|q|\alpha_{s}^{+}(1 + \mathrm{e}^{-2a\alpha_{s}^{+}}) = 2|q|\alpha_{s}^{+}\widehat{U}\mathrm{e}^{-a\alpha_{s}^{+}} + \frac{1}{\mu^{+}}\widehat{T}^{H}(1 - \mathrm{e}^{-2a\alpha_{s}^{+}}).$$

Back in the time and space domains, we obtain (see Appendix A)

$$\frac{1}{c_{s}^{+}}\dot{u}^{H}(x,t) = \frac{2}{c_{s}^{+}}\dot{u}\left(x, t - \frac{H}{c_{s}^{+}}\right) + f^{H}(x,t) + \frac{1}{\mu^{+}}\tau^{H}(x,t) - \frac{1}{\mu^{+}}\tau^{H}\left(x, t - \frac{2H}{c_{s}^{+}}\right) + h^{H}(x,t)$$

$$-\frac{1}{c_{s}^{+}}\dot{u}^{H}\left(x, t - \frac{2H}{c_{s}^{+}}\right) - g^{H}(x,t)$$

$$= l^{H}(x,t), \tag{B.1}$$

where the convolution terms are expressed in the Fourier domain as

$$F^{H} = \mathscr{F}(f^{H}) = -|q|aU\left(t - \frac{H}{c_{s}^{+}}\right) + 2|q|\int_{\frac{H}{c_{s}^{+}}}^{t} C'_{H3}(|q|c_{s}^{+}t')U(t - t')|q|c_{s}^{+}\,\mathrm{d}t',$$

$$H^{H} = \mathscr{F}(h^{H}) = \frac{1}{\mu^{+}}\int_{\frac{2H}{c_{s}^{+}}}^{t} D_{3}(|q|c_{s}^{+}t')T^{H}(t - t')|q|c_{s}^{+}\,\mathrm{d}t',$$

$$G^{H} = \mathscr{F}(g^{H}) = -|q|aU^{H}\left(t - \frac{2H}{c_{s}^{+}}\right) + |q|\int_{0}^{t}\left(C_{\infty}(|q|c_{s}^{+}t') + C_{H3}(|q|c_{s}^{+}t')\right)U^{H}(t - t')|q|c_{s}\,\mathrm{d}t'.$$

The convolution kernels $D_{3}(T)$, $C_{H3}(T)$, $C_{\infty}(T)$ have been defined in (8) and (13), and

$$C'_{H3}(T) = \left(\frac{J_{1}\left(\sqrt{T^{2} - a^{2}}\right)}{\sqrt{T^{2} - a^{2}}} + a^{2}\frac{J_{2}\left(\sqrt{T^{2} - a^{2}}\right)}{T^{2} - a^{2}}\right)H(T - a).$$

A modal stability and precision analysis similar to that presented in Sections 4.2 and 4.3 shows that the numerical implementation of relation (B.1) suffers from the same instability as the spectral formulation used the interface quantities. These instabilities can therefore be eliminated by using the same first-order low-pass filter as that described by (18).

References

[1] Yu HH, He MY, Hutchinson JW. Edge effects in thin film delamination. Acta Mater 2001;49:93–107.

[2] Thouless MD. Fracture mechanics for thin film adhesion. IBM J Res Dev 1994;38:367–77.

[3] Kim KS, Kim J. Elasto-plastic analysis of the peel test for thin film adhesion. J Engng Mater Technol—Trans ASME 1988;110(3):266–73.

[4] Zhuk AV, Evans AG, Hutchinson JW, Whitesides GM. The adhesion energy between polymer thin films and self-assembled monolayers. J Mater Res 1998;13(12):3555–64.

[5] Vossen JL. Measurements of film–substrate bond strength by laser spallation. Adhes Measur Thin Films, Thick Films Bulk Coat 1978;640:122–3.

[6] Gupta V, Argon AS, Parks JA, Ans Cornie DM. Measurement of interface strength by a laser spallation technique. J Mech Phys Solids 1992;40:141–80.

[7] Yuan J, Gupta V. Measurement of interface strength by the modified laser-spallation technique: I. Experiment and simulation of the spallation process. J Appl Phys 1993;74:2388–96.

[8] Gupta V, Yuan J, Pronin A. Recent developments in the laser spallation technique to measure the interface strength. J Adhes Sci Technol 1994;8:713–47.

[9] Wang J, Weaver RL, Sottos NR. A parametric study of laser induced thin film spallation. Exp Mech 2002;42(1):74–83.

[10] Wang J, Weaver RL, Sottos NR. Mixed-mode failure of thin films using laser generated shear waves. Exp Mech 2003;43(3):323–30.

[11] Wang J, Weaver RL, Sottos NR. Laser induced decompression shock development in fused silica. J Appl Phys 2003;93(12):9529–36.

[12] Wang J, Weaver RL, Sottos NR. Tensile and mixed-mode strength of a thin film–substrate interface under laser induced pulse loading. J Mech Phys Solids 2004;52:999–1022.

[13] Wang J. Thin film adhesion measurement by laser induced stress waves. PhD thesis. Urbana IL: Department of Theoretical and Applied Mechanics, University of Illinois; 2002.

[14] Morrissey JW, Geubelle PH. A numerical scheme for mode 3 dynamic fracture problems. Int J Numer Meth Engng 1997;40:1181–96.

[15] Geubelle PH, Breitenfeld MS. Numerical analysis of dynamic debonding under anti-plane shear loading. Int J Fract 1997;85:265–82.

[16] Geubelle PH, Rice JR. A spectral method for three-dimensional elastodynamic fracture problems. J Mech Phys Solids 1995;43(11):1791–824.

[17] Breitenfeld MS, Geubelle PH. Numerical analysis of dynamic debonding under 2d in-plane and 3d loading. Int J Fract 1998;93:13–38.

[18] Cochard A, Rice JR. A spectral method for numerical elastodynamic fracture analysis without spatial replication of the rupture event. J Mech Phys Solids 1997;45(8):1393–418.